Acoustic and Ultrasonic Detection With Radio-Frequency Encoded Fiber Laser Sensors

Bai-Ou Guan, *Member, IEEE*, Long Jin, Linghao Cheng, *Member, IEEE*, and Yizhi Liang

(Invited Paper)

***Abstract*—Fiber lasers have been exploited as sensors for the detection of extremely weak mechanical parameters, by monitoring the radio-frequency beat signal between orthogonal polarized lasing modes. This sensor scheme has presented advantages including advanced measurement capability, low cost and convenience in signal demodulation, resistance to environmental disturbances, and intrinsic multiplexing capability. Here, we demonstrate the capability of the fiber laser sensors for the detection of low-frequency ($<$2 kHz) acoustic waves and ultrasound signals at frequency ranges $>$1 MHz (denoted as "high frequency" in this paper) and around 200 kHz (denoted as "medium frequency"), toward different applications. For low-frequency acoustic sensing, the detection limit reaches 74 μPa/Hz$^{1/2}$ at 1 kHz which is comparable to the zeroth-order sea noise. For high-frequency ultrasound detection, the laser sensor presents a detection capability of 40 Pa over 50 MHz bandwidth, which allows its application as an ultrasound detector in photoacoustic (PA) imaging. Preliminary three dimensional PA imaging is presented, by means of time-to-space reconstruction. Ultrasound detection with a polymer-packaged fiber laser at 100 kHz range is demonstrated, which could find applications in underwater search and targeting. Its imaging capability is also exhibited.**

***Index Terms*—Acoustic sensors, ultrasound sensors, optical fiber sensors, fiber lasers.**

I. Introduction

ACOUSTIC detection is a fundamental technique for engineering applications. Optical fiber hydrophones, i. e., underwater fiber optic acoustic sensors working at frequencies typically $<$10 kHz, have played an important role over the last two decades as an alternative to the existing piezoelectrical sensors, due to their high sensitivity, immunity to electromagnetic interference and multiplexing capability [1]–[17]. They have been widely used in military applications, ocean physics researches and resource explorations. Interferometric fiber hydrophones with schemes including Mach-Zehnder, Sagnac or Michelson interferometers have been implemented with high sensitivity taking advantage of phase detection [1]–[3]. A sensor array can be formed with tens to hundreds of such sensors [4], [5]. Extrinsic Fabry-Perot (F-P) cavities can detect acoustic waves, taking advantage of pressure induced deflection of the diaphragm [6]–[11]. Metal and silica diaphragms and photonic crystal cavities have been integrated at fiber tip as pressure-deformable elements [6]–[9]. Recently, an F-P acoustic sensor based on a single- or few-layered graphene diaphragm has been exhibited with advanced measurement capability [10], [11]. Alternatively, fiber laser hydrophones have demonstrated great performance in acoustic detection. This sensing scheme can be considered as a derivation from the conventional interferometric sensor schemes, by placing the single-longitudinal-mode fiber lasers at wet end as sensing elements [12]–[15]. The imbalanced interferometer, on the other hand, read out the variation of lasing frequencies. This sensing scheme presents great compactness and can maintain the intrinsic wavelength multiplexing capability [16], [17].

The fiber laser sensors can also work in an alternative encoding manner. A sufficiently short laser naturally emits single-colored output with two orthogonal polarized modes and offers a beat signal in radio-frequency domain. The beat signal can respond to external perturbations in terms of frequency variation [18]–[21]. In this paper, we demonstrate radio-frequency encoded fiber laser sensors for underwater detection of acoustic and ultrasound waves. A corrugated diaphragm is used for the transduction of low-frequency acoustic wave into concentrated load on the laser cavity to induce a beat-frequency change. A detection limit of $74\,\mu\mathrm{Pa}/\mathrm{Hz}^{1/2}$ at 1 kHz has been achieved, which is comparable to the 0th-order sea noise, as a result of the concentration effect of the transducer as well as the self-compensated noise of the beat signal. On the other hand, the detection of ultrasound waves at frequencies over 1 MHz has been of particular interests for medical imaging applications. The measurement capability of conventional piezoelectrical sensor is proportional to detection area. This readily limits applications such as endoscopy where small sensor size and high sensitivity are simultaneously required. In addition,

Manuscript received June 1, 2016; revised November 1, 2016; accepted November 24, 2016. Date of publication December 9, 2016; date of current version March 14, 2017. This work was supported in part by the National Natural Science Foundation of China under Grants 61235005 and 11474133, in part by Guangdong Natural Science Foundation under Grant S2013030013302, and in part by the Department of Education, Guangdong Province under Grant Yq2013021.

The authors are with Guangdong Provincial Key Laboratory of Optical Fiber Sensing and Communications, Institute of Photonics Technology, Jinan University, Guangzhou 510632, China (e-mail: tguanbo@jnu.edu.cn; iptjinlong@gmail.com; Chenglh@ieee.org; liangyizhi88528@gmail.com).

Color versions of one or more of the figures in this paper are available online at http://ieeexplore.ieee.org.

Digital Object Identifier 10.1109/JSTQE.2016.2635035

piezoelectric sensors may also be ferroelectric, which are susceptible to electromagnetic disturbances. A number of photonic and optical approaches for ultrasound detection have been proposed, which exhibit high sensitivity and small sizes [22]–[26]. Most of them rely on the detection of acoustically induced resonance shift of an optical resonator with Fabry-Perot or microring geometries. High-performance fiber optic ultrasound detector (intrinsic or extrinsic) is desired towards applications in photoacoustic endoscopy, taking advantage of its line profile [27]–[29]. Although the ultrasonically induced optical delay/birefringence change in an optical fiber has been observed decades ago [30], [31], the application of optical fibers in ultrasonic detection is rather limited. The acoustic wavelength at this frequency regime is comparable to fiber diameter and it is difficult to constructively induce an optical response due to the acoustic-phase nonuniformity on arrival at the fiber. Particularly, for photoacoustic imaging, conventional interferometric approach presents a relatively poor sensitivity because of the limited effective interaction length. In this paper, we have investigated the response of a radio-frequency encoded fiber laser sensor to both planar and spherical acoustic waves. The laser sensor can present a noise-equivalent pressure (NEP) of 40 Pa over 50 MHz bandwidth. Preliminary result in photoacoustic microscopy has been demonstrated. Based on the scaling law between the acoustic wavelength and fiber diameter, the fiber laser based ultrasonic detection is extended down to hundreds of kHz ranges, by using polymer packaged fiber lasers. Ultrasonic detection at these frequencies can find applications in the underwater targeting and search, security monitoring in power facilities, as well as medical imaging [32], [33]. The effect of the packaging is to efficiently excite mechanical modes at these frequencies to obtain desired optical response. Its application in ultrasound imaging is also exhibited. This result indicates that the working frequency band of a fiber laser based ultrasound sensor can be controlled by changing the sensor transverse dimension, yielding great flexibility in sensor design and implementation.

The paper is organized as follows: Section II describes the fabrication and working principle of the radio-frequency encoded fiber laser sensor. The general sensitivity characteristics and noise figure have been investigated in detail. Theoretical analysis suggests that both sensitivity and noise are largely dependent on the effective cavity length, which is associated with laser parameters including grating length, separation and the coupling strength of the grating reflectors. The analysis in this section provides useful guidance for the following acoustic/ultrasound sensing. In Section III we demonstrate the detection of low-frequency acoustic waves with a fiber laser and the assistance of a corrugated diaphragm. The diaphragm translates acoustic pressure into a concentrated load on the laser cavity and induces detectable beat-frequency variation. The detection limit reaches a level comparable to the 0th order sea noise. In Section IV we exhibit the inherent capability of a bare fiber laser for the detection of broadband ultrasound signals. By utilizing this ability we further demonstrate its application in photoacoustic (PA) imaging, which is a fast growing imaging modality in medical care and diagnoses. The fiber laser approach is promising for future PA endoscopic applications, taking advantage of its optical transparency, high sensitivity, broad working bandwidth, high compactness, and large field of view. In addition, we demonstrate that the working band can be shift to around hundreds of kHz by using a polymer-packaged fiber laser. Its imaging capability is further exhibited. In Section V we draw a conclusion.

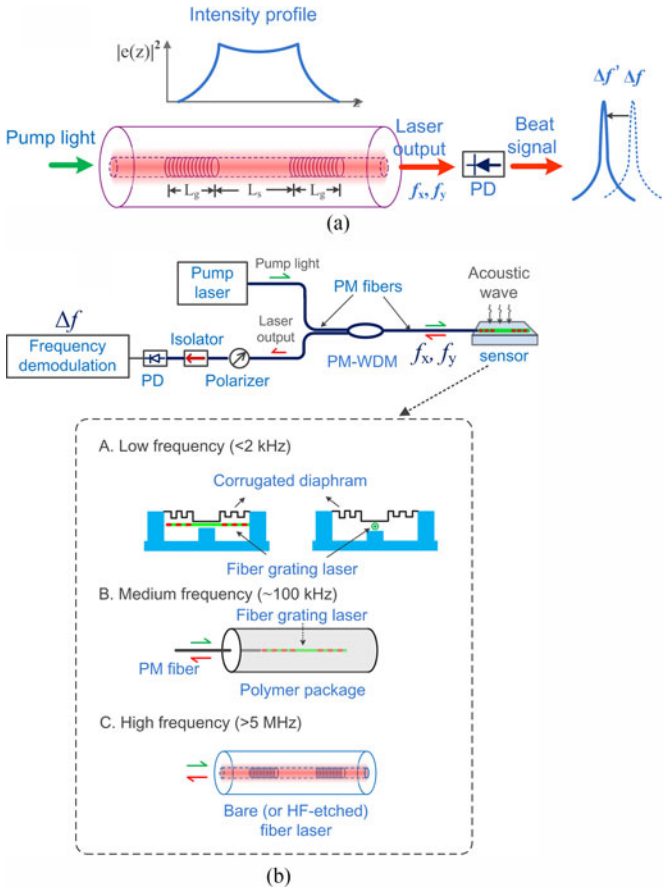

Fig. 1. (a) Schematic of the radio-frequency encoded fiber laser sensor. (b) Experimental setup for acoustic and ultrasonic detection. WDM: Wavelength division multiplexer. PM fibers: Polarization-maintaining fibers. PD: Photodetctor.

II. The Sensing Element

A. Fabrication and Working Principle of the Fiber Laser Sensor

Fig. 1(a) shows the schematic of the sensing element, i. e., a fiber grating laser, fabricated by photoinscribing two wavelength-matched, highly reflective intracore Bragg gratings in series in a rare-earth doped fiber. Each grating has a length of L_{g} and the grating separation is L_{s}. The cavity naturally emits two orthogonal polarization lasing modes, as a result of the intrinsic birefringence. The resonant condition for each polarization mode can be expressed by [20], [34]

$$\frac{4\pi}{c} f_{x,y} \int_{-\infty}^{+\infty} n_{x,y}(z)|e(z)|^2 \mathrm{d}z = 2M\pi \tag{1}$$

where $f_{\mathrm{x,y}}$ is the lasing frequency for each polarization mode, $n_{\mathrm{x,y}}$ denotes their effective indexes, M is the resonant order and c denotes the speed of light in vacuum. The term $|e(z)|^2$

represents the longitudinal profile of intracavity light intensity, normalized via $\int_{-\infty}^{+\infty}|e(z)|^2\mathrm{d}z=1$. A beat note can be observed in radio-frequency (RF) domain and the beat frequency can be expressed by

$$\Delta f = \frac{c}{n_0\lambda}\int_{-\infty}^{+\infty} B(z)|e(z)|^2\mathrm{d}z \tag{2}$$

where $B(z)$ is the local birefringence. The birefringence is introduced in the fiber drawing process, which is a mainly a result of the deviation from perfect circular core geometry [35]. The thermal stress induces an additive birefringence, which is associated with the resultant nonuniform strains over the fiber core [35], [36]. The intrinsic birefringence can be considered invariant along the fiber. At the grating regions, the local birefringence can be changed as a result of the UV side illumination and therefore the resultant beat frequency can be somewhat different for the individual lasers fabricated in the same fiber, because the fiber principle axis may be not known prior to the laser fabrication. The output beat frequency can be greatly changed via heat treatment by use of CO_2 laser side irradiation for multiplexing purposes [37]. Alternatively, the beat signal can also be continuously adjusted with a tuning range of up to 15 GHz for microwave photonics applications, by applying transverse load along the principal axis [38].

Fig. 1(b) shows the experimental setup for the acoustic and ultrasonic detection. A CW 980 nm laser diode is used to pump the cavity via a wavelength division multiplexer. The pump absorption is about 20 dB/m to offer sufficient gain for laser oscillation. The fiber lasers are fabricated by inscribing two wavelength-matched Bragg gratings in a photosensitive Er-doped fiber, by use of a 193 nm pulsed ArF excimer laser and a phase mask with a pitch of 1059 nm. The formation of index modulation relies on photosensitivity associated with two-step excitation. Each grating has a coupling strength of above 25 dB to provide strong optical feedback. The grating separation is typically less than 1 cm to force single-longitudinal-mode output. The fiber laser is annealed at 120 °C for two hours for relaxation of internal stress induced by UV exposure. The two polarization modes beat at the photodetector and the beat frequency is measured by a vector signal analyzer. An isolator is used to prevent unwanted endface reflections. A polarizer is employed to maximum the intensity of the beat signal. Polarization-maintaining fibers are used for stabilization of the frequency and intensity of the beat signal.

Fig. 2 shows the output optical spectrum of the laser measured with a high-resolution (10 MHz) optical spectrum analyzer. The pump power is typically tens of mW to saturate the laser output. As a result, the two polarization modes have comparable output powers and the mode competition is weak due to the polarization-burning-hole effect. A stable beat spectrum can be obtained, as shown in Fig. 2(b). The beat frequency is 2.74 GHz, corresponding to an intrinsic birefringence of 2.05×10^{-5}.

The fiber laser sensor presents detectable frequency shift in response to applied acoustic waves. The frequency-modulated signal can be demodulated based on a method similar to that in the software-defined radio systems. The modulated signal is mixed with two low-noise quadrature radio frequency signals which have identical frequencies close to the carrier. After this

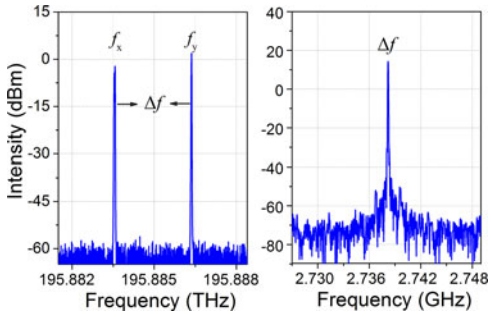

Fig. 2. Optical spectrum of the laser output measured with a high-resolution optical spectrum analyzer (left) and the spectrum of the beat signal (right).

quadrature down conversion we can have two baseband signals $I(t)$(In-phase)and $Q(t)$ (quadrature).The phase information of the beat signal can be extracted via $\theta(t) = \arctan(Q(t))/(I(t)))$. The frequency modulated signal can be subsequently recovered by processing the phase data in a differentiator.

B. Beat signal stabilization.

Evidence shows that the pump instability in intensity, wavelength, and polarization can induce variation in lasing frequencies [39]. In contrast, we found that the beat signal is highly susceptible to polarization variation of the pump light. The output beat frequency presents a sinusoidal change with the orientation angle with a range of 18 MHz [40]. This effect is attributed to the resonantly enhanced nonlinearity, which is a nonlinearity effect associated with ion population distribution in different levels. The contrast between the lasing intensities along the two orthogonal polarizations varies with the orientation angle and causes a birefringence change. The resultant beat frequency change can be expressed by [41]

$$\Delta(\Delta f) = \frac{c}{n_0\lambda_0} I_{\mathrm{p}}(1-\eta)\beta\cos 2\theta \tag{3}$$

where I_{p} is the pump intensity, η is a coefficient between zero and unity which measures the gain difference between the two polarization modes, β denotes the dependence of index change on lasing intensity. The use of polarization-maintaining fibers to guide the pump light can effectively stabilize the beat frequency. The frequency fluctuation can be reduced from 1.5 MHz to about 150 kHz as a result of polarization control. The annealing process can reduce the orientation-dependant frequency variation from 18 to 4 MHz, due to the reduction of gain difference. This process can help stabilize the output beat frequency.

Another major instability factor is the endface reflection. This optical feedback can interfere with the intracavity light and modulates the equivalent cavity loss. The random changes in phase and amplitude can cause gain (or loss) fluctuation. Here we assume the reflected state of polarization can be preserved, the maximum variation of beat-frequency as a result of the feedback (when the phase difference between the feedback and intracavity lights varies from 0 to π as a result of the environmental perturbations) can be written as [41]:

$$\Delta\upsilon_{b,\max} \cong \frac{\kappa c}{n\pi} rT\sqrt{1+a_b^2} \tag{4}$$

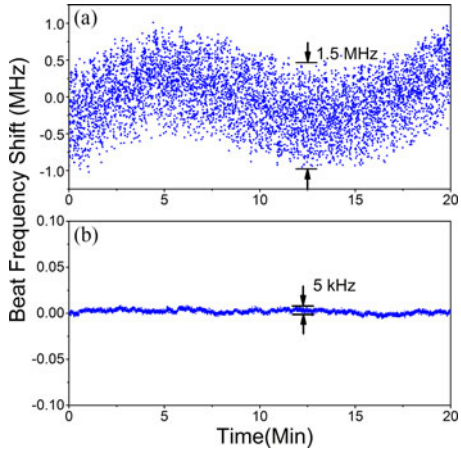

Fig. 3. Measured beat-frequency fluctuations over 20 min before (a) and after (b) stabilization treatments including annealing, polarization stabilization and prevention of optical feedbacks [40].

where the a_{b} is the linewidth enhancement factor for beat-frequency, r is the external reflectivity, T is the transmissivity of the Bragg grating which is close to unity, κ is the grating coupling coefficient. Substituting $r = 4\%$ and $T = 1$, the frequency fluctuation can be calculated as more than 1 MHz. In order to weaken the effect of the optical feedback, we use an isolator and burn the reflection endface to prevent possible reflections. Fig. 3 shows the measured beat-frequency fluctuation before and after the stabilization processes including annealing, the use of PM fibers as well as the prevention of unwanted optical feedbacks. The fluctuation is significantly reduced from 1.5 MHz to 5 kHz [42]. The treatments also help stabilize the intensity of the beat signal. The intensity fluctuation over 20 min is within ± 1 dB [40].

C. Intrinsic Sensitivity

Suppose an external perturbation creates a birefringence change with a longitudinal profile $\delta B(z)$, the induced beat frequency change can be written as

$$\delta(\Delta f) = \frac{c}{n_0 \lambda} \int_{-\infty}^{+\infty} \delta B(z) |e(z)|^2 \mathrm{d}z \tag{5}$$

Eq. (5) suggests that the fiber laser can respond to an external perturbation provided that it can change the intracavity birefringence. It is well known that external forces can deform the fiber and establish a stress distribution. As a result of the photoelastic effect, stress induces anisotropic changes of refractive index within the fiber and creates birefringence. The induced change in mode indices can write as $n_{\mathrm{x}} = n_{\mathrm{x}0} - p_{11}\sigma_{\mathrm{x}} - p_{12}(\sigma_{\mathrm{y}} + \sigma_{\mathrm{z}})$ and $n_{\mathrm{y}} = n_{\mathrm{y}0} - p_{11}\sigma_{\mathrm{y}} - p_{12}(\sigma_{\mathrm{x}} + \sigma_{\mathrm{z}})$, where $n_{\mathrm{x0,y0}}$ represents the mode indices with no applied stress, $\sigma_{\mathrm{x,y,z}}$ denotes normal strains, p_{11} and p_{12} are the photoelastic coefficients of silica [43]. The corresponding birefringence change can be expressed by

$$\Delta B = (p_{12} - p_{11})(\sigma_x - \sigma_y) \tag{6}$$

The induced birefringnence change can be obtained with the knowledge of the stress distribution over the fiber, specifically, in the core. A straightforward approach to induce birefringence change is to subject a transverse force F $(\mathrm{N/m})$. The induced birefringence can be expressed by [43], [44]

$$\Delta B = \Gamma \cdot F \tag{7}$$

where Γ is a coefficient mainly determined by the elastic properties of the glass fiber via $\Gamma = 2n_0^3(p_{12} - p_{11})(1 + v_p)/\pi r_{\mathrm{f}} E$, where E and v_{p} denote the Young's modulus and Poisson's ratio of silica glass, r_{f} is fiber radius. For a more complicated structure, for instance, a nonuniform packaged laser sensor described in [45], the stress/strain distribution can be calculated with numerical methods. In addition, the laser can present a beat-frequency change in response to magnetic field, as a result the induced circular birefringence by magneto-optic effect [46]. This issue will not be discussed in detail in the current paper. The change in average index n_0 or lasing wavelength λ can possibly induce a beat-frequency change, based on Eq. (2), but the contribution is too weak to be taken into consideration.

Eq. (5) also suggests that the optical response is weighted by intracavity intensity density $|e(z)|^2$. Fig. 4(a) shows measured longitudinal profiles of transverse load sensitivity for lasers with different cavity lengths, which is performed with a load-scanning method [34]. In the measurement the transverse load is applied on laser cavity along the principle axis via point contact manner and induces a highly localized birefringence change. Based on Equation (6), the beat-frequency shift induced by a normal point force N at position z can be written

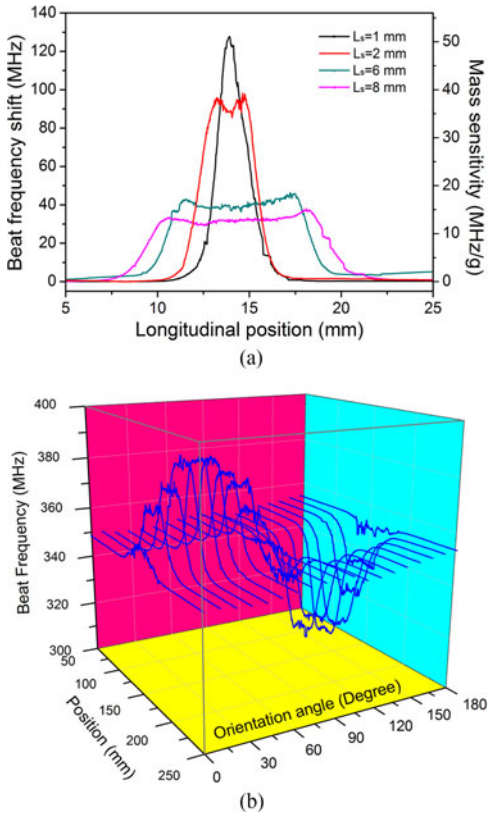

Fig. 4. (a) Measured spatial sensitivities for fiber grating lasers with different cavity lengths. (b) Measured responses to transverse load in terms of beat frequency change for a fiber grating laser with a grating separation of 4 mm with different loading orientations [34].

as

$$\delta(\Delta f) = \frac{c}{n_0 \lambda} \Gamma \eta \cdot N \tag{8}$$

The product $\frac{c}{n_0\lambda}\Gamma$ has an amplitude of about 10 GHz/(N/mm), and can be somewhat different for different fibers as a result of the core asymmetry. The factor η is the normalized local intensity density which can be expressed by $\eta = \lim_{L_c \to 0} \int_{-L_c/2}^{+L_c/2} |e(z)|^2 \mathrm{d}z / L_c$. By scanning the load position along the fiber length with a step of 20 microns, the sensitivity profile (or the laser mode profile) can be plotted. Fig. 4(a) suggests that the lasers with $L_s = 8$, 6 and 2 mm present flat-top profiles with two peaks at the inner edges of the gratings. The one with $L_s = 1\,\mathrm{mm}$ presents only one peak in the sensitivity profile. It presents a sensitivity as high as 51.1 MHz/g (or 51.9 GHz/N) at the peak, as a result of the more confined light in cavity. The 8-mm fiber laser, in comparison, presents an average sensitivity of 12 MHz/g (or 1.22 GHz/N) over the blank region in between the gratings.

The spatial sensitivity profile is related to the parameters including grating separation, fiber gain and grating coupling strength. Specifically, the profile over the blank segment in between the gratings is largely determined by the gain of the rare-earth doped fiber. The forward and backward lights experience amplifications over the blank region in between the two gratings and reaches intensity maxima before arriving at the gratings. As a result, the Fabry-Perot fiber laser typically presents a profile with two peaks at the inner grating edges. Fibers with high gains can create sharper peaks and those with low gain lead to flat-top profiles. In addition, for the curves over the gratings, higher coupling strengths enable higher slopes. Based on the coupled mode theory [44], the intensities rapidly decrease over the gratings with a simple relation $T = 1 - \tanh^2(\kappa z)$ where κ represents the coupling coefficient and z represents the penetration depth.

The lasers with $L_s = 8$, 6 and 2 mm can be approximately considered as Fabry-Perot lasers, with rectangular mode profiles written as

$$|e(z)|^2 = \begin{cases} \frac{1}{L_s} & -\frac{L_s}{2} < z < \frac{L_s}{2} \\ 0 & \text{other regions} \end{cases} \tag{9}$$

This model assumes that the intracavity light is evenly confined by the grating reflectors. This model is reasonable considering the low gain and extremely high grating reflectivities. The induced response to applied transverse load N is written as $\delta(\Delta f) = \frac{c\Gamma}{n_0\lambda} \cdot \frac{N}{L_s}$. That means the sensitivity is inversely proportional to the grating separation L_s and explains why longer cavities present lower beat-frequency shifts. The measured spatial sensitivities (color curves in Fig. 4(a)) shows reasonable deviations from ideal rectangular profiles. First, the sensitivities are higher at the inner edge of the gratings than the central region due to light amplification along both forward and backward directions. Second, the sensitivities decrease with a certain rate along the outwards directions, rather than an abrupt change. This is a result of the limited grating coupling strengths.

The sensitivity profiles of shorter cavities (e.g., $L_s = 1\,\mathrm{mm}$) can be approximately treated as an ideal DFB structure, which is almost lossless and the gratings have infinite lengths. The normalized intensity profile can be expressed by [47], [48]

$$|e(z)|^2 = \kappa \cdot e^{-2\kappa|z|} \tag{10}$$

where κ is the coupling coefficient of the gratings. The maximum sensitivity apparently appears at $z = 0$, where the beat-frequency shift is $\delta(\Delta f) = \frac{c\Gamma}{n_0\lambda} \cdot N\kappa$. Therefore, its spatial sensitivity presents a single-peak profile (black curve in Fig. 4(a)), with maximum sensitivity at the central position of the laser.

Although varying cavity length enables different mode profiles and the corresponding sensitivity distributions, the fiber lasers can be generally characterized by the effective cavity length L_{eff}. The effective length approximately equals to the grating separation for Fabry-Perot lasers and can be expressed as $L_{\mathrm{eff}} = 1/\kappa$ for the DFB structure. For simplicity, the maximum sensitivity to a point load can be considered scale with the reciprocal of L_{eff}.

Fig. 4(b) shows the measured sensitivity profiles for a laser with individual loading orientations, to give a full picture of the spatial sensitivity.The longitudinal sensitivity is profiled for each loading orientation with a rotation step of 10 degrees. The grating separation is about 4 mm. The maximum frequency shifts appear at the fast axis (45° in Fig. 4) and slow axis (135°), respectively. The induced optical response is related to the loading direction as a result of core asymmetry [21]. Based on the perturbation theory, the right-hand side of Eq. (5) should multiply $\sin(2\theta)$ where θ denotes the orientation angle, provided that the applied perturbation can hardly change the orientation of the principle axis. The measured result in Fig. 4(b) indicates that one should determine the principle axis of the laser sensor for maximum sensitivity in practical uses.

D. Noise

The dominate noise source of a fiber grating laser is the intracavity thermal fluctuation which writes as $\Delta T(t, \vec{r})$ (or $\Delta T(\omega, \vec{r})$ in frequency domain). Based on Eq. (5), the noise spectrum can be expressed as

$$S_{\mathrm{noise}}(f) = (\Delta v_{\mathrm{noise}})^2 = \frac{c^2}{n_0^2 \lambda_0^2} s^2(\vec{r}) \left\langle \Delta T(\omega, \vec{r}) \Delta T(\omega', \vec{r}\,') \right\rangle \tag{11}$$

where $s(\vec{r})$ measures the sensitivity in terms of frequency change to a localized temperature variation. Its amplitude is not uniform over the fiber cross section due to the possiblethermal stress relaxation in addition to the thermo-optic effect. The correlation function can be further written as [49]

$$\begin{aligned} &\left\langle \Delta T(\omega, \vec{r}) \Delta T(\omega', \vec{r}\,') \right\rangle \\ &= \int_\infty |e(z)|^2 dz \int_\infty |e(z')|^2 \Delta T(\omega, \vec{r}) \Delta T(\omega', \vec{r}\,') \\ &\quad M^2(x,y) M^2(x',y') \mathrm{d}s \mathrm{d}s' \mathrm{d}z' \\ &= \Delta T^2 \int_\infty |e(z)|^2 dz \int_\infty |e(z')|^2 \delta(z - z') \mathrm{d}z' \\ &= \Delta T^2 \int_\infty |e(z)|^4 dz \end{aligned} \tag{12}$$

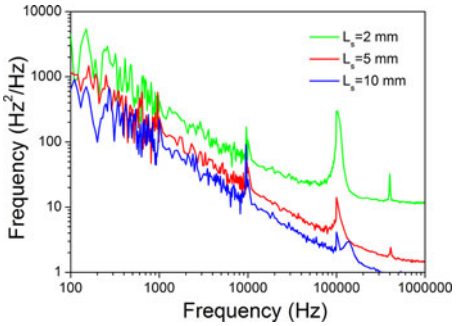

Fig. 5. Measured frequency noise spectra of output beat signal with different cavity lengths. All the lasers are fabricated in the same fiber.

Based on the theory illustrated in [49] by Foster *et al*, the correlation degree between two selected points exponentially declines with their distance and thermal variations at different positions can be approximately considered uncorrelated. Eq. (12) indicates that the thermally induced frequency fluctuation $\Delta v_{\mathrm{noise}}$ scales with $1/\sqrt{L_{\mathrm{eff}}}$ for a fiber laser. Fig. 5 shows the measured spectral density profiles of frequency noise for lasers with different cavity lengths. All the lasers are fabricated in the same Er-doped fiber. The individual lasers present $1/f$ profiles (at low and medium frequency regimes) a result of the nonequilibrium thermal fluctuations [47–49]. The individual noise spectra present different levels. Here we define a factor C to depicts the noise level and write the noise spectral density as $S(f) = C/f$. Estimated from the result in Fig. 5, the amplitudes of this factor are $C_1 = 2.5 \times 10^5 (\mathrm{Hz}^2)$, $C_2 = 1.1 \times 10^5\ (\mathrm{Hz}^2)$ and $C_3 = 0.7 \times 10^5 (\mathrm{Hz}^2)$ for cavity separations $L_{\mathrm{s}} = 2, 5$, and 10 mm, respectively. The noise level roughly presents inverse proportion to effective cavity length, in agreement with the above theory.

The two orthogonally lasing modes share the same laser cavity and have a high correlation. As a result, the thermal noise of the beat signal is much lower than each polarization mode. This has been demonstrated in [47] and verified in our previous experiment, but the noise compensation mechanism is not fully clear yet. In addition, refs. [47]–[49] described that the random thermal fluctuation scales with ions density. In order to achieve lower noise level, we have attempted to select an Er-doped fiber out of the available products with lower ion concentration, provided that the lasing oscillation can be established. For comparison, lasers are fabricated in an Er-Yb co-doped fiber with identical cavity parameters. The fiber has greatly higher dopant concentration and the pump absorption is higher than 500 dB/m. As a result, they present noise levels10-fold higher than those in the Er-doped fiber.

E. Strategies for Different Perturbation Forms

The induced response in beat-frequency variation can be calculated with Eq. (5), regardless how the perturbations are subjected on the sensor. However, in practical applications, one should consider the specific forms of the perturbations for better detection capability. The design and implementation of sensors can be classified into the following cases for each form of perturbation:

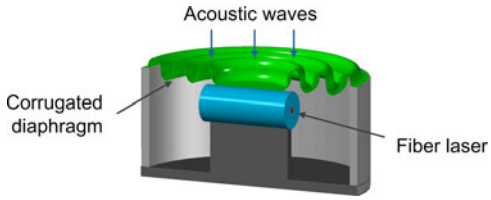

Fig. 6. Schematic of the transducer based on a corrugated diaphragm which converts acoustic pressure into concentrated transverse load on the fiber laser.

The first type of perturbation is a uniform field. In this model, the induced birefringence change is invariant along fiber length over the laser cavity, and Eq. (3) can be simplified as $\delta(\Delta f) = \frac{c}{n_0 \lambda}\delta B$. That means the sensitivity is not relevant with specific laser mode profile. This model applies for acoustic detection at medium frequency range (several tens to hundreds of kHz) with a polymer packaged fiber laser. As a result, longer cavities are preferred for lower noise level as long as single longitudinal mode output can be ensured.

The second type is the localized perturbation, that is, the load is approximately subjected via point contact. As described in above text, a DFB-like laser can offer higher sensitivity provided that the load is subjected at the phase-shift point, due to the highly confined mode profile. Combining the dependences of sensitivity and noise on the effective length, shorter cavity length also yield higher signal-to-noise level (scaling with $1/\sqrt{L_{\mathrm{eff}}}$), which corresponds to better measurement capability. This model applied for the detection of photoacoustical signals, since the effective interaction length is comparable to acoustic wavelength and can be considered as a point-like load.

The third case is the regional perturbation which is distributed over a certain segment of the laser cavity. For simplicity, we assume that the load is evenly distributed over the length L_{c}. the corresponding beat frequency shift can be expressed by

$$\delta(\Delta f) = \frac{c\Gamma N}{n_0 \lambda}\gamma \tag{13}$$

where $\gamma = \int_{-L_{\mathrm{c}}/2}^{+L_{\mathrm{c}}/2} |e(z)|^2 \mathrm{d}z / L_{\mathrm{c}}$ represents the average normalized light intensity density over the loaded region.

III. Detection of Low-Frequency Acoustic Waves

Fig. 6 schematically shows the transducer structure for the detection of low-frequency acoustic waves with a fiber laser sensor in beat-frequency encoded manner. The transduction of acoustic signals into optical response relies on a corrugated diaphragm. The metal corrugated diaphragm is a basic elastic element and has been exploited as external pressure sensitive device e. g., microphones, for engineering applications, also can be used for the purposes as medium isolation and elastic bracing. For an edge-clamped diaphragm, acoustic pressure can induce a reflection at the rigid center. Here we place the sensing element—fiber laser beneath and in lateral contact with the diaphragm. As a result, the acoustic pressure can be transduced into the transverse stress over the laser cavity and induce a beat-frequency shift.

Considering that the acoustic wavelength at this regime is much larger than the dimension of the diaphragm, the acoustic

response can be treated as a hydrostatic problem. The deflection of a flat, edge rigidly clamped, circular diaphragm under a pressure difference can be approximately expressed by [50]

$$\frac{PR^4}{Eh^4} = A\left(\frac{y}{h}\right) + B\left(\frac{y^3}{h^3}\right) \tag{14}$$

where y represents the induced center deflection, P denotes uniformly distributed pressure difference across the diaphragm, E is the Young's modulus of the metal, h and R are the thickness and radium of the diaphragm, respectively. The parameters $A = 5.33/(1 - v^2)$ and $B = 2.38/(1 - v^2)$ are two constants which are associated with the Poisson's ratio v. The corrugated diaphragm can be equivalently treated as a plane one with modified amplitudes of A and B, expressed by [51]

$$A_{\mathrm{p}} = \frac{2(3+q)(1+q)}{3(1-\frac{v^2}{q^2})} \text{ and } B_{\mathrm{p}} = \frac{32(q+6-v)}{(q+3)^2(q-v)} \tag{15}$$

where $q^2 = 1 + 1.5H^2/h^2$ for shallow sinusoidal profiles along the radial direction and H represents the corrugation depth. However, for the structure in Fig. 6, the central region of the diaphragm is also supported which zero deflection. We can equivalently consider the central region is loaded with an upward concentrated force F_{b} and totally compensate the deflection induced by the applied pressure P. The relation between them can write as $F_{\mathrm{b}} = -PA_{\mathrm{eff}}$. The effective area can be expressed by [51]

$$A_{\mathrm{eff}} = \frac{1+q}{2(3+q)}\pi R^2 \tag{16}$$

For a thin diaphragm q typically has an amplitude over 10 and the effective area approaches $\frac{1}{2}\pi R^2$. Therefore, the effect of the diaphragm is to convert the acoustic pressure P into an concentrated force F_{b} with an amplification factor which equals half area of the diaphragm. For the diaphragm-based transducer used in the experiment, the reacting force is applied over a limited length which can be approximate as a point load.

The corrugated diaphragm is made of Beryllium copper, which has radius of 19 mm, a thickness of 200 μm, and a corrugation depth of 2 mm. The acoustic response of the fiber laser acoustic sensor has been tested in a water tank. A calibrated acoustic source is employed to generate acoustic signals approximate to plane waves. Fig. 7 shows the measured beat-frequency deviation as a function of applied acoustic pressure. In Fig. 7 inset we demonstrate a typical sensor output in terms of beat-frequency variation measured with a 3-mm fiber laser. Fig. 8 shows the measured frequency responses of fiber laser sensors with different grating separations. Measured result suggests that shorter laser cavities enable higher acoustic sensitivities, as a result of the more confined laser mode profile. This acoustic sensor fits the second case described in Section II-E. The average sensitivity for the 3-mm fiber laser over the working band is about 180 kHz/Pa. The minimal detectable signal is estimated as 74 μPa/Hz$^{1/2}$ at 1 kHz, based on the measured sensitivity and the frequency noise in Fig. 5. The detection limit is comparable to the 0th order sea noise. The fundamental natural frequency is about 1300 Hz, which is determined by the elastic properties and corrugation geometry.

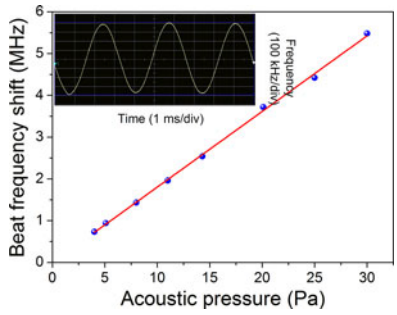

Fig. 7. Measured beat-frequency deviation as a function of applied acoustic pressure at 800 Hz. This test is carried out with a 3-mm laser sensor. Inset: A typical output signal in response to acoustic wave.

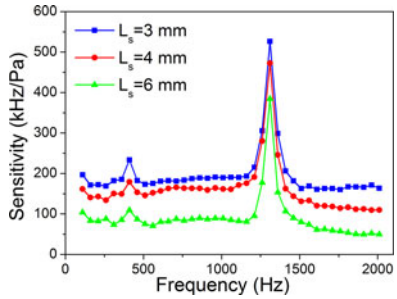

Fig. 8 Measured frequency response of the diaphragm-based fiber laser acoustic sensors, with grating separations 3, 4 and 6 mm, respectively.

IV. Ultrasound Detection and Imaging

Ultrasound waves with acoustic wavelengths comparable to the fiber diameter can induce strong interaction with the optical fiber, resulting in detectable phase changes [30], [31], [52]. This interaction can be treated as a problem of the scattering of obliquely incident plane wave from a homogeneous cylinder with infinite length submerged in a fluid [53], [54]. The decoupled Helmholtz equations, which describe the behaviors of the acoustic waves, are solved in cylindrical coordinates by using elastic potentials:

$$\begin{aligned} \Delta\varphi + \varphi k_l^2 &= 0 \\ \Delta\boldsymbol{\Psi} + \boldsymbol{\Psi} k_t^2 &= 0 \end{aligned} \tag{17}$$

where φ and ψ denote the scalar and vector potentials and k_{l} and k_{t} are the longitudinal and shear wave numbers. The general solutions of Eq. (17) can be expressed by

$$\begin{aligned} \varphi &= \mathrm{e}^{\mathrm{i}(k_z z - \omega t)} \sum_{\mathrm{n}=-\infty}^{+\infty} A_{\mathrm{n}} J_{\mathrm{n}}(k_{\mathrm{lr}} r) \\ \Psi_{\mathrm{t1}} &= \mathrm{e}^{\mathrm{i}(k_z z - \omega t)} \sum_{\mathrm{n}=-\infty}^{+\infty} B_{\mathrm{n}} J_{\mathrm{n}}(k_{\mathrm{tr}} r) \\ \Psi_{\mathrm{t2}} &= \mathrm{e}^{\mathrm{i}(k_z z - \omega t)} \sum_{\mathrm{n}=-\infty}^{+\infty} C_{\mathrm{n}} J_{\mathrm{n}}(k_{\mathrm{tr}} r) \end{aligned} \tag{18}$$

where J_{n} denotes the n-th Bessel functions. The solutions should have included counterparts Neumann functions but they have

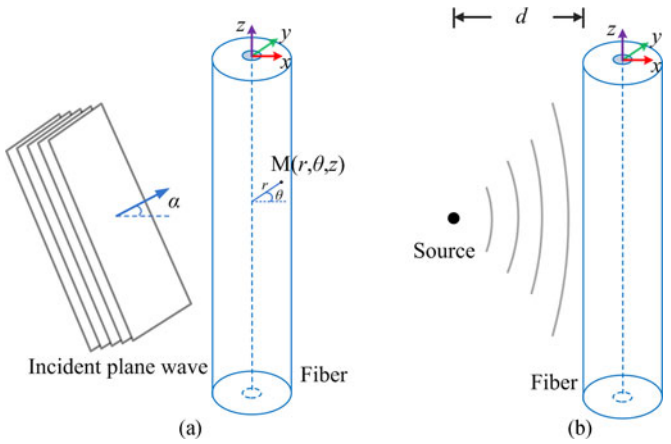

Fig. 9. Geometries of incident plane wave (a) and spherical wave (b) on the optical fiber.

been ignored due to the singular requirement at $r = 0$. The incident wave can be depicted as

$$\varphi_{\rm inc} = {\rm e}^{{\rm i}(k_z z - \omega t)} \sum_{\rm n=-\infty}^{+\infty} {\rm i}^{\rm n} J_{\rm n}(k_{\rm lr} r) e^{{\rm in}\theta} \tag{19}$$

where ω represents angular frequency of the incident plane wave and θ denotes the azimuthal angle. Then the complex amplitudes $A_{\rm n}$, $B_{\rm n}$ and $C_{\rm n}$ of the scattered waves can be determined by using the boundary conditions which depict displacement/stress continuity at the water/fiber interface. The scattered waves can establish nonuniform stresses over the optical fiber and induces changes in refractive index as well as fiber elongation. The acoustically induced birefringence change $\delta B_{\rm p}$ can be subsequently obtained based on Eq. (6).

The responses of the fiber lasers to ultrasound plane waves are first measured. Ultrasound pulses generated by an unfocused ultrasound transducer (V358-SU, Panametrics) are normally launched on the fiber laser and the beat frequency change is monitored. The result has been calibrated with a commercial hydrophone. Fig. 10(a) and (b) exhibit the measured temporal and frequency responses of a 125-μm fiber laser. A number of sensitivity maxima can be observed, corresponding to the individual in-plane mechanical modes. The temporal signal presents a long oscillating tail, as a result of the strong interaction with the vibration mode at 40 MHz. These mechanical modes can be generally described as Bessel functions with azimuthal indices $n = 0$ and 2 (Other indexes can not fulfill the boundary conditions and can be ignored). Zero azimuthal index leads to isotropic stresses at fiber core and can hardly induces a birefringence change. In contrast, the second order azimuthal modes produce stresses along the orthogonal directions $\varepsilon_{\rm x}$ and $\varepsilon_{\rm y}$ with opposite signs and is dominantly responsible for the induced birefringence change. These modes are analogy to the fiber being harmonically squeezed at frequency ω. The individual peaks in Fig. 10(b) are all attributed to the second azimuthal modes. The first two peaks at 22 and 40 MHz corresponds to the 1st and 2nd radial modes (their potentials are described as 1st and 2nd order Bessel functions). Note that the large difference in Pockel's constants $p_{11} = 0.26$ and $p_{12} = 0.12$ offers an

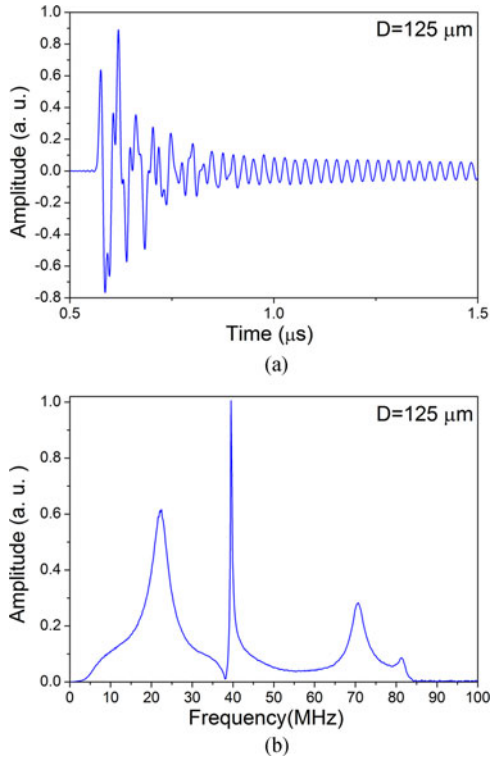

Fig. 10. Measured temporal response (a) and frequency spectrum (b) of a 125 μm fiber laser ultrasound detector.

additive enhancement in the transduction of acoustic pressure to beat frequency change. The frequency response curve is a function of the ratio of the fiber diameter over acoustic wavelength. That means one can shift the mechanical resonant frequencies by changing the diameter of the fiber detector. The oscillating tail in Fig. 10(a) can cause unwanted shadow effect for imaging applications and needs to remove. This is done by reducing the fiber diameter via hydrofluoric acid (HF) etching. Fig. 11 shows the measured response of a 60-μm fiber laser. The initial peak at 22 MHz is shifted to 42 MHz and the higher-order modes move out of the detectable frequency range. In addition, the thinner fiber laser presents a broader bandwidth, which yields a finer axial resolution. As a result, a much shorter pulse can be obtained, as shown in Fig. 11(a). The 65-μm fiber laser presents a beat-frequency shift of 198 MHz in response to 88 kPa acoustic pressure, yielding a sensitivity of $2.25\,{\rm MHz/kPa}$. The noise-equivalent-pressure (NEP) of the detector is estimated as 40 Pa in 50 MHz bandwidth, considering the noise floor at about 83 kHz.

Here we demonstrate the application of the fiber laser ultrasound detector in an optical-resolution photoacoustic microscopy (OR-PAM). In a typical PAM system, laser pulses with ns width are delivered to a tissue. The light is partially absorbed which induces a local temperature rise and the generation of broadband ultrasound waves. By detecting the ultrasound signals, the original optical energy deposition in the tissue can be mapped [55]–[57]. Fig. 12 shows the schematic of the OR-PAM system by use of a bare fiber laser ultrasonic detector. Here two human hair are submerged in water and prepared as

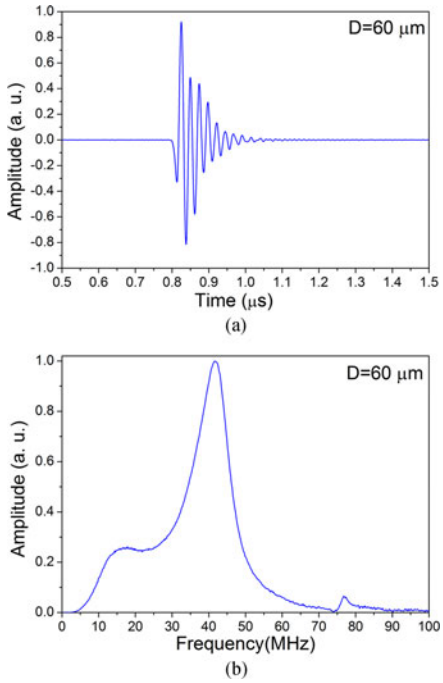

Fig. 11. Measured temporal response (a) and frequency spectrum (b) of a 60 μm fiber laser ultrasound detector. The fiber has been HF-etched to reduce the fiber diameter.

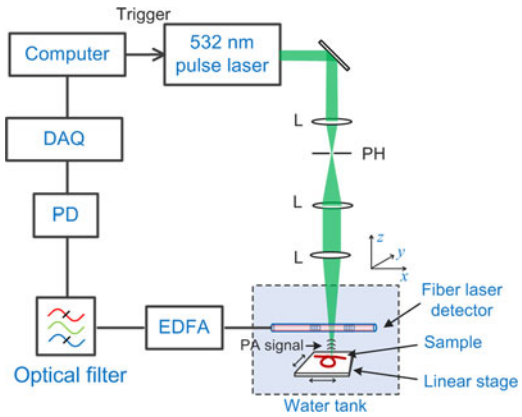

Fig. 12. Experimental setup for OR-PAM with a fiber laser ultrasound probe. EDFA: Erbium-doped fiber amplifier. PD: Photodetector. L: Lens. PH: Pinhole. DAQ: Data acquirement system.

sample by assembling them in a knot geometry. A 532-nm pulsed laser delivers light to the sample to excite photoacoustic signals. The single pulse energy can vary from tens of nanojoules to about 100 nJ. The pulse width is about 1.8 ns. The fiber laser ultrasound detector is placed near the sample to probe the photoacoustic signals. The axial distribution (along z axis) of optical absorptance is reconstructed by time-to-space mapping and the imaging resolution is limited by the bandwidth of the detector (Note that the coordinate system here is defined in accordance with the traditional ways in optical imaging). The sample is mounted on a 2-axis linear stage to scan along the x axis with a step of 6.6 μm and y axis with a step of 18 μm. The photoacoustic signal is recorded during the scanning to yield a three-dimensional image. Fig. 13 shows the imaging result. The image is rotated at different angles to show the 3-D imaging

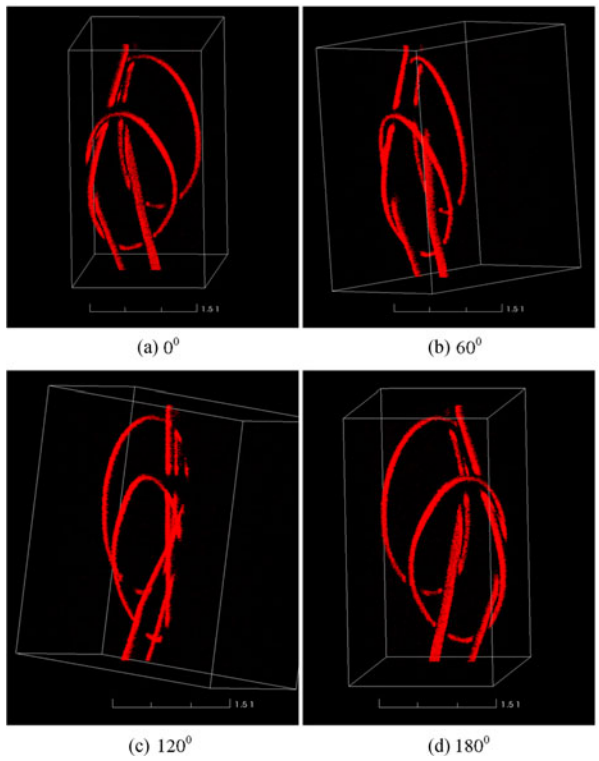

Fig. 13. PAM images of two hairs in knot geometry at different view angles.

capability. The optical-diffraction limited lateral resolution is 3.2 μm, by using an objective with a numerical aperture of 0.1. The axial resolution is 130μm, limited by the bandwidth of the ultrasound sensor.

Photoacoustic imaging involves the detection of spherical ultrasound waves from a point source, which is challenging for fiber optic sensors. Fig. 9(b) schematically shows the detection of photoacoustic signals using a fiber laser detector. The spherical wave at frequency ω generated at point (d, z_0), where d denotes the source-to-fiber distance and z_0 denotes the position at the fiber length direction with respect to the middle point of the laser cavity. The spherical wave can be considered as an extension of plane waves with different incident angles α [53], [54]. The individual plane wave components arrive at the line detector with different amplitudes and phases. The incident wave at position z at the line detector can write as $p_0(\omega, \alpha(z))\frac{e^{-ik_{\mathrm{L}}r(z)}}{r(z)}$, where $\alpha = \mathrm{arctg}(\frac{|z-z_0|}{d})$ represents the incident direction of this component, $r = \sqrt{|z-z_0|^2 + d^2}$ is the distance from the acoustic source. Utilizing Eq. (5), the induced beat frequency change is an integration result over the laser cavity, which is expressed by

$$\delta(\Delta f) = \frac{c}{n_0 \lambda}\int_{-L/2}^{+L/2} \delta B(\omega, \alpha(z))\frac{e^{-ik_{\mathrm{L}}r(z)}}{r(z)}|e(z)|^2 \mathrm{d}z \quad (20)$$

where $\delta B(\omega, \alpha)$ is the induced birefringence change by plane wave $p_0(\omega, \alpha)$. Eq. (20) can reflect the difficulties in the detection of photoacoustic signals by use of an integrated detector with a line profile. First, at positions far away from the source, the incident powers of acoustic waves are extremely low (the amplitude scales with the reciprocal of the distance) and their

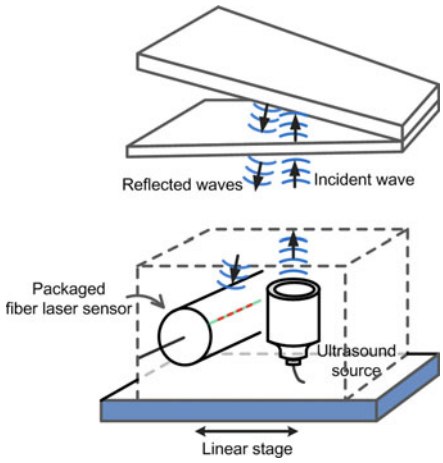

Fig. 14. Experimental setup for ultrasound imaging with a polymer-packaged fiber laser.

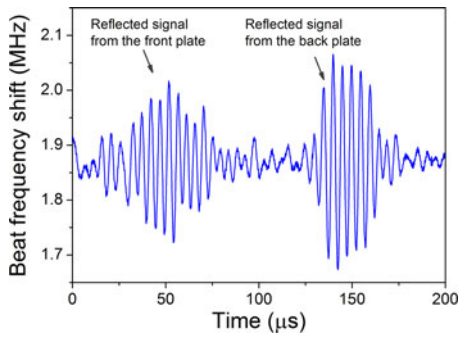

Fig. 15. Measured temporal response of the reflected ultrasound signals from the front and back covers.

contributions can be ignored. Second, even at positions near the source, the resultant response can be significantly weakened due to the compensation due to the variation in phase at different positions. As a result, the effective interaction length is limited. Consider an extreme case that the source-fiber distance d approaches zero, the effective interaction length equals $\lambda_a/2$, where λ_a represents acoustic wavelength at frequency ω. That is close to a "point" contact manner described in Section II, and the conventional strategy by taking advantage of phase accumulation for sensitivity enhancement does not apply. The feasibility of photoacoustic detection and imaging by use of such a fiber laser relies on its responsivity to a point load. In order to further enhance the acoustic sensitivity, we need to attempt to reduce the effective cavity length to raise the intracavity intensity density. An Erbium doped fiber amplifier has been applied for the amplification of the output laser signal and enhancement of signal-to noise ratio. The detection capability is limited by the noise of the photodetector, since the noise of the output beat signal becomes extremely low over this frequency range.

Fig. 1(b) shows the schematic of the polymer-packaged fiber laser for the ultrasound detection at frequencies around hundreds of kHz. The polymer is made of acrylic acid epoxy resin, which is in fluid state at room temperature and turns into solid when blended with hardener. The fiber laser is fixed in a tank before the blend is poured into it. After 24 h at room temperature, the polymer becomes a hard block. It can be further polished

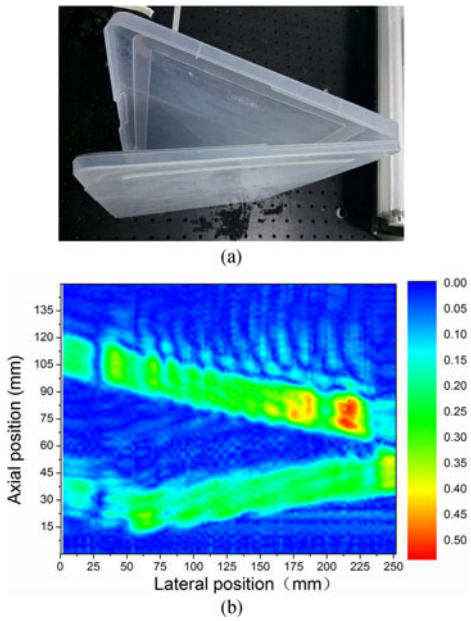

Fig. 16. Photograph (a) and ultrasound image (b) of an open plastic box. The ultrasound imaging relies on the time-to-space reconstruction of the reflected waves detected by the packaged fiber laser. The central frequency of the ultrasound source is 200 kHz [58].

to have a cylindrical geometry. The diameter of the polymer package is $D = 5$ mm. The effect of polymer packaging is to shift the resonant frequency of the first-order radial mode to hundreds of kHz order, based on the scaling law between the acoustic wavelength and the detector size. As a result, the vibration can be effectively excited by incident ultrasound waves at this frequency range. The fiber laser is squeezed by the polymer and presents a frequency shift. Fig. 14 shows the experimental setup for ultrasound imaging with the packaged fiber laser sensor. Plane-wave pulsed ultrasound signals are generated from a source with a central frequency at 200 kHz. An open plastic box is submerged in water and taken as sample. The incident waves are reflected at the front and back covers of the box. The reflected waves can be detected by the packaged fiber laser. Fig. 15 shows a typical response in terms of beat-frequency variation. By scanning the ultrasound source and the packaged detector simultaneously at different lateral positions, the sample can be imaged via time-to-space mapping. Fig. 16 exhibits the photograph as well as the ultrasound image of the sample. The spatial resolution is currently limited by the bandwidth of the ultrasound source. Ultrasound detection at this frequency range can find applications in underwater search and targeting, as well as the arc discharge monitoring in transformers.

V. Conclusion

In conclusion, we have demonstrated the capability of beat-frequency encoded fiber laser sensors in the detection of low-frequency (<2 kHz) acoustic waves and ultrasound signals at high-frequency (>1MHz) and medium-frequency (200 kHz) ranges. For low-frequency acoustic detection, a diaphragm-based sensing configuration is proposed to translate the acoustic pressure into transverse load on the laser cavity, to induce a detectable beat-frequency change. A corrugated diaphragm is used

instead of a plane one for sensitivity enhancement and broad working bandwidth. As a result, a detection limit comparable to the 0th order sea noise has been achieved. In contrast, a bare fiber laser presents inherent sensitivity to high-frequency ultrasound waves, due to the strong interaction between the incident waves and the silica fiber. The detection limit characterized by NEP reaches 40 Pa over 50 MHz, which suggests its capability in response to weak broadband ultrasound signals. Such as laser sensor has been exploited as ultrasound detector in an OR-PAM image system, to obtain a 3-D image via time-to-space mapping. The working frequency band is further shifted to around 200 kHz, by packaging the laser in a polymer cylinder, whose ultrasound imaging capability is also experimentally demonstrated.

The demodulation of frequency/wavelength for conventional fiber laser sensors typically relies on the use of an imbalanced Mach-Zenhder interferometer to extract the phase changes. However, this technique is quite complicated and has difficulties in dealing with disturbances associated with polarization variations. In comparison, the beat-frequency encoded fiber laser sensors works in a self-heterodyning manner. For simplicity, one of the polarization mode (say, x-polarization) can be taken as a reference signal, and the other mode (y-polarization mode) acts as the "sensing" signal. The frequency (or phase) demodulation of the heterodyning signal becomes much easier by using conventional processing techniques in coherent communications and microwave technologies. On the other hand, it maintains advantages of conventional fiber laser sensors or fiber optic sensors, e. g., intrinsic multiplexing capability. In addition, evidence has shown that the output beat signal has a much lower frequency noise level than each polarization mode, due to the effective self compensation. For some applications with strong unwanted perturbations such as environmental temperature fluctuation or vibrations, additional frequency locking technique is required for the wavelength-encoded sensors. In contrast, the self-compensation manner also helps the beat-frequency encoded counterpart avoid the requirements of frequency locking or stabilization processes to overcome these issues.

Acknowledgment

The authors would like to thank Dr. L. Wang for the useful discussions in photoacoustic imaging. The authors would also like to thank Z. Quan, M. Li, Q. Yuan, F. Zhou, D. Liu, W. Yang, and X. Bai for their contributions.

References

[1] J. A. Bucaro, H. D. Dardy and E. F. Carome, "Fiber-optic hydrophone," *J. Acoust. Soc. Amer.*, vol. 62, no. 5, pp. 1302–1304, 1977.

[2] C. K. Kirkendall and A. Dandridge, "Overview of high performance fibre-optic sensing," *J. Phys. D, Appl. Phys.*, vol. 37, no. 18, pp. R197–R216, 2004.

[3] B. Culshaw and A. Kersey, "Fiber-optic sensing: A historical perspective," *J. Lightw. Technol.*, vol. 26, no. 9, pp. 1064–1078, May 2008.

[4] R. I. Crickmore *et al.*, "Remotely pumped and interrogated 96 channel fibre-optic hydrophone array," in *Proc. 16th Opt. Fibre Sensor Conf. Tech. Dig.*, 2003, pp. 760–763.

[5] J. P. Dakin, C. A. Wade, and M. Henning, "Novel optical fibre hydrophone array using a single laser source and detector," *Electron. Lett.*, vol. 20, no. 1, pp. 53–54, 1984.

[6] J. Xu, X. Wang, K. L. Cooper, and A. Wang, "Miniature all-silica fiber optic pressure and acoustic sensors," *Opt. Lett.*, vol. 30, no. 24, pp. 3269–3271, 2005.

[7] D. Donlagic and E. Cibula, "All-fiber high-sensitivity pressure sensor with SiO_2 diaphragm," *Opt. Lett.*, vol. 30, no. 12, pp. 2071–2073, 2005.

[8] F. Xu *et al.*, "High-sensitivity Fabry–Pérot interferometric pressure sensor based on a nanothick silver diaphragm," *Opt. Lett.*, vol. 37, no. 2, pp. 133–135, 2012.

[9] O. Kilic, M. Digonnet, G. Kino, and O. Solgaard, "External fibre Fabry–Pérot acoustic sensor based on a photonic-crystal mirror," *Meas. Sci. Technol.*, vol. 18, no. 10, pp. 3049–3054, 2007.

[10] J. Ma, W. Jin, H. L. Ho, and J. Y. Dai, "High-sensitivity fiber-tip pressure sensor with graphene diaphragm," *Opt. Lett.*, vol. 37, no. 13, pp. 2493–2495, 2012.

[11] J. Ma *et al.*, "Fiber-optic Fabry–Pérot acoustic sensor with multilayer graphene diaphragm," *IEEE Photon. Technol. Lett.*, vol. 25, no. 10, pp. 932–935, May 2013.

[12] G. A. Cranch, G. M. H. Flockhart, and C. K. Kirkendall, "Distributed feedback fiber laser strain sensors," *IEEE Sensors J.*, vol. 8, no. 7, pp. 1161–1172, Jul. 2008.

[13] S. Foster, A. Tikhomirov, M. Milnes, J. V. Velzen, and G. Hardy, "A fibre laser hydrophone," *Proc. SPIE*, vol. 5855, pp. 627–630, 2005.

[14] W. Zhang, Y. Liu, F. Li, and H. Xiao, "Fiber laser hydrophone based on double diaphragms: Theory and experiment," *J. Lightw. Technol.*, vol. 26, no. 10, pp. 1349–1352, May 2008.

[15] L. Ma, Y. Hu, H. Luo, and Z. Hu, "DFB fiber laser hydrophone with flat frequency response and enhanced acoustic pressure sensitivity," *IEEE Photon. Technol. Lett.*, vol. 21, no. 17, pp. 1280–1282, Sep. 2009.

[16] S. Foster *et al.*, "A 16 channel fibre laser sensor array," in *Proc. Aust. Conf. Opt. Fiber Technol./Aust. Opt. Soc.* , 2006, pp. 40–42, Paper FA4.

[17] D. J. Hill *et al.*, "Fibre laser hydrophone array," *Proc. SPIE*, vol. 3860, pp. 55–66, 1999.

[18] B.-O. Guan, L. Jin, Y. Zhang, and H. Y. Tam, "Polarimetric heterodyning fiber grating laser sensors," *J. Lightw. Technol.*, vol. 30, no. 8, pp. 1097–1112, Apr. 2012.

[19] J. T. Kringlebotn, W. H. Loh, and R. I. Laming, "Polarimetric Er3+-doped fiber distributed-feedback laser sensor for differential pressure and force measurements," *Opt. Lett.*, vol. 21, no. 22, pp. 1869–1871, 1996.

[20] B.-O. Guan, Y. Tan, and H. Tam, "Dual polarization fiber grating laser hydrophone," *Opt. Express*, vol. 17, no. 22, pp. 19544–19550, 2009.

[21] Y. Zhang, B. O. Guan, and H. Y. Tam, "Characteristics of the distributed Bragg reflector fiber laser sensor for lateral force measurement," *Opt. Commun.*, vol. 281, no. 18, pp. 4619–4622, 2008.

[22] E. Zhang, J. Laufer, and P. Beard, "Backward-mode multiwavelength photoacoustic scanner using a planar Fabry–Perot polymer film ultrasound sensor for high-resolution three-dimensional imaging of biological tissues," *Appl. Opt.*, vol. 47, no. 4, pp. 561–577, 2008.

[23] T. Ling, S. L. Chen, and L. J. Guo, "High-sensitivity and wide-directivity ultrasound detection using high-Q polymer microring resonators," *Appl. Phys. Lett.*, vol. 98, no. 20, 2011, Art. no. 204103.

[24] H. Li, B. Dong, Z. Zhang, H. F. Zhang, and C. Sun, "A transparent broadband ultrasonic detector based on an optical micro-ring resonator for photoacoustic microscopy," *Sci. Rep.*, vol. 4, 2013, Art. no. 4496.

[25] S. M. Leinders *et al.*, "A sensitive optical micro-machined ultrasound sensor (OMUS) based on a silicon photonic ring resonator on an acoustical membrane," *Sci. Rep.*, vol. 5, 2014, Art. no. 14328.

[26] A. Rosenthal, D. Razansky, and V. Ntziachristos, "High-sensitivity compact ultrasonic detector based on a pi-phase-shifted fiber Bragg grating," *Opt. Lett.*, vol. 36, no. 10, pp. 1833–1835, 2011.

[27] A. Rosenthal, *et al.*, "Sensitive interferometric detection of ultrasound for minimally invasive clinical imaging applications," *Laser Photon. Rev.*, vol. 8, no. 3, pp. 450–457, 2014.

[28] B. Dong, S. Chen, Z. Zhang, C. Sun, and H. F. Zhang, "Photoacoustic probe using a micro-ring resonator ultrasonic sensor for endoscopic applications," *Opt. Lett.*, vol. 39, no. 15, pp. 4372–4375, 2014.

[29] E. Z. Zhang, and P. C. Beard, "A miniature all-optical photoacoustic imaging probe," *Proc. SPIE*, vol. 7899, 2011, Art. no. 78991F.

[30] R. P. Depaula, L. Flax, J. H. Cole, and J. A. Bucaro, "Single-mode fiber ultrasonic sensor," *J. Quantum Electron.*, vol. QE-18, no. 4, pp. 680–683, 1982.

[31] L. Flax, J. H. Cole, R. P. De Paula, and J. A. Bucaro, "Acoustically induced birefringence in optical fibers," *J. Opt. Soc. Amer.*, vol. 72, no. 9, pp. 1159–1162, 1982.

[32] H. Wen, D. G. Wiesler, A. Tveten, B. Danver, and A. Dandridge, "High-sensitivity fiber-optic ultrasound sensors for medical imaging applications," *Ultrasonic Imaging*, vol. 20, no. 2, pp. 103–112, 1998.

[33] M. MacAlpine, Z. Zhao, and M. S. Demokan, "Development of a fibre-optic sensor for partial discharges in oil-filled power transformers," *Elect. Power Syst. Res.*, vol. 63, no. 1, pp. 27–36, 2002.
[34] F. Zhou, L. Jin, Y. Liang, L. Cheng, and B.-O. Guan, "Spatial sensitivity characterization of dual-polarization fiber grating laser sensors," *J. Lightw. Technol.*, vol. 33, no. 19, pp. 4151–4155, Oct. 2015.
[35] S. Rashleigh, "Origins and control of polarization effects in single-mode fibers," *J. Lightw. Technol.*, vol. 1, no. 2, pp. 312–331, Jun. 1983.
[36] L. Jin, Y.-N. Tan, Z. Quan, M.-P. Li, and B.-O. Guan, "Strain-insensitive temperature sensing with a dual polarization fiber grating laser," *Opt. Express*, vol. 20, no. 6, pp. 6021–6028, 2012.
[37] L. Jin, Y. Liang, M.-P. Li, L. Cheng, and B.-O. Guan, "A 16-element multiplexed heterodyning fiber grating laser sensor array," *J. Lightw. Technol.*, vol. 32, no. 22, pp. 3808–3813, Nov. 2014.
[38] Q. Yuan, Y. Liang, L. Jin, L. Cheng, and B.-O. Guan, "Implementation of a widely tunable microwave signal generator based on dual-polarization fiber grating laser," *Appl. Opt.*, vol. 54, no. 4, pp. 895–900, 2015.
[39] E. Rønnekleiv, "Frequency and intensity noise of single frequency fiber Bragg grating lasers," *Opt. Fiber Technol.*, vol. 7, no. 3, pp. 206–235, 2001.
[40] Y. Liang, Q. Yuan, L. Jin, L. Cheng, and B.-O. Guan, "Effect of pump light polarization and beat note stabilization for dual-polarization fiber grating laser sensors," *IEEE J. Sel. Topics Quantum Electron.*, vol. 20, no. 5, Sep./Oct/ 2014, Art. no. 5600208.
[41] E. Rønnekleiv, M. Ibsen, and G. J. Cowle, "Polarization characteristics of fiber DFB lasers related to sensing applications," *IEEE J. Quantum Electron.*, vol. 36, no. 6, pp. 656–664, Jun. 2000.
[42] Y. Liang, L. Jin, Q. Yuan, L. Cheng, and B.-O. Guan, "Detection of an extremely small mass with a dual-polarization fiber grating laser," *Proc. SPIE*, vol. 9157, 2014, Art. no. 91571C.
[43] A. Yariv and P. Yeh, "*Photonics: Optical Electronics in Modern Communications*, 6th ed. London, U.K.: Oxford Univ. Press, 2006.
[44] R. Gafsi and M. A. El-Sherif, "Analysis of induced-birefringence effects on fiber Bragg gratings," *Opt. Fiber Technol.*, vol. 6, no. 3, pp. 299–323, 2000.
[45] L. Jin, Z. Quan, L. Cheng, and B.-O. Guan, "Hydrostatic pressure measurement with heterodyning fiber grating lasers: Mechanism and sensitivity enhancement," *J. Lightw. Technol.*, vol. 31, no. 9, pp. 1488–1494, May 2013.
[46] L. Cheng, J. Han, Z. Guo, L. Jin, and B.-O. Guan, "Faraday-rotation-based miniature magnetic field sensor using polarimetric heterodyning fiber grating laser," *Opt. Lett.*, vol. 38, no. 5, pp. 688–690, 2013.
[47] S. Foster, "Spatial mode structure of the distributed feedback fiber laser," *IEEE J. Quantum Electron.*, vol. 40, no. 7, pp. 884–892, Jul. 2004.
[48] S. Foster and A. Tikhomirov, "Experimental and theoretical characterization of the mode profile of single-mode DFB fiber lasers," *IEEE J. Quantum Electron.*, vol. 41, no. 6, pp. 762–766, Jun 2005.
[49] S. Foster, "Low-frequency thermal noise in optical fiber cavities," *Phys. Rev. A*, vol. 86, 2012, Art. no. 043801.
[50] P. R. Scheeper, W. Olthuis and P. Bergveld, "The design, fabrication, and testing of corrugated silicon nitride diaphragms," *J. Microelectromech. Syst.*, vol. 3, no. 1, pp. 36–42, 1994.
[51] M. Di Giovanni, *Flat and Corrugated Diaphragm Design Handbook*. Boca Raton, FL, USA: CRC Press, 1982.
[52] B.-O. Guan, H. Y. Tam, S. T. Lau and H. L. W. Chan, "Ultrasonic hydrophone based on distributed Bragg reflector fiber laser," *IEEE Photon. Technol. Lett.*, vol. 17, no. 1, pp. 169–171, Jan. 2004.
[53] T. Berer *et al.*, "Characterization of broadband fiber optic line detectors for photoacoustic tomography," *J. Biophoton.*, vol. 5, no. 7, pp. 518–528, 2012.
[54] I. A. Veres *et al.*, "Characterization of the spatio-temporal response of optical fiber sensors to incident spherical waves," in *Proc. IEEE Int. Ultrason. Symp.*, 2014, vol. 135, no. 4, pp. 1853–1862.
[55] J. Yao and L. V. Wang, "Photoacoustic microscopy," *Laser Photon. Rev.*, vol. 7, no. 5, pp. 758–778, 2013.
[56] J. Yao and L. V. Wang, "Sensitivity of photoacoustic microscopy," *Photoacoustics*, vol. 2, no. 2, pp. 87–101, 2014.
[57] J. Yao *et al.*, "High-speed label-free functional photoacoustic microscopy of mouse brain in action," *Nature Methods*, vol. 12, no. 5, pp. 407–410, 2015.
[58] D. Liu *et al.*, "Highly sensitive fiber laser ultrasound hydrophones for sensing and imaging applications," *Opt. Lett.*, vol. 41, no. 19, pp. 4530–4533, 2016.

Bai-Ou Guan (M'08) received the B.Sc. degree in applied physics from Sichuan University, Chengdu, China, in 1994, and the M.Sc. and Ph.D. degrees in optics from Nankai University, Tianjin, China, in 1997 and 2000, respectively. From 2000 to 2005, he was with the Department of Electrical Engineering, Hong Kong Polytechnic University, Hong Kong, first as a Research Associate, and then as a Postdoctoral Research Fellow. From 2005 to 2009, he was with the School of Physics and Optoelectronic Engineering, Dalian University of Technology, Dalian, China, as a Full Professor. In 2009, he joined Jinan University, Guangzhou, China, where he founded the Institute of Photonics Technology. His current research interests include fiber optic devices and technologies, optical fiber sensors, biomedical photonic sensing and imaging, and microwave photonics. He has authored and coauthored more than 130 papers in the peer-reviewed international journals and presented 50 invited talks at international and national conferences. He received the Distinguished Young Scientist Grant from the Natural Science Foundation of China in 2012. He is a member of OSA, and has served as the General Chair/Co-Chair, Technical Program Committee or Subcommittee Chair/Co-Chair for over ten international conferences.

Long Jin received the B.S. and Ph.D. degrees from Nankai University, Tianjin, China, in 2003 and 2008, respectively. He joined the Department of Electrical Engineering, Hong Kong Polytechnic University in 2008, as a Research Assistant and then as a Postdoctoral Research Fellow. Since 2010, he has been with the Institute of Photonics Technology, Guangzhou, China as an Associate Professor. He has published more than 50 journal and conference papers. His research interests include fiber optic devices and sensors.

Linghao Cheng (S'04–M'07) received the B.S. and Ph.D. degrees from the University of Electronic Science and Technology of China, Chengdu, China, and Nanyang Technological University, Singapore, in 2000 and 2007, respectively. In 2000, he joined Wuhan Research Institute of Post and Telecommunication, Hubei, China, as a Research and Development Engineer for two years. He is currently a Professor in the Institute of Photonics Technology, Jinan University, Guangzhou, China. His research interests include optical communications and optical fiber sensing.

Yizhi Liang received the B.S. degree from Guangdong University of Technology, Guangzhou, China, in 2012. He is currently working toward the Ph.D. degree in the Institute of Photonics Technology, Jinan University, Guangzhou, China. His research interests include fiber optic sensors and photoacoustic imaging.